Large-scale pore network and continuum simulations of solute longitudinal dispersivity of a saturated sand column

Mojtaba G. Mahmoodlu [a,b,*], Amir Raoof [b], Tom Bultreys [c], Jeroen Van Stappen [c], Veerle Cnudde [c]

[a] Department of Water Engineering, Gonbad Kavous University, Iran
[b] Deparement of Earth Sciences, Utrecht University, Utrecht, the Netherlands
[c] Department of Geology, PProGRess-UGCT, Ghent University, Belgium

ARTICLE INFO

ABSTRACT

Predicting the solute dispersivity in porous media is complicated by the known scale dependency of dispersion processes. In this study, we combined three complementary methods to investigate solute dispersivity at different length scales. The applied methods included 36-cm long column experiments, extremely large three-dimensional (3D) X-ray image-based pore network simulations, and Darcy scale modelling. We used X-ray imaging to extract the information on pore structures needed to construct a very long, 36-cm, pore network model. Doing so, for the first time, a direct comparison of the pore-scale model to the large experimental observations was performed. The longitudinal dispersivity was found to increase with length, with the rate of increase being lower at higher flow velocities. Results have shown that a pore network, which matches pore connectivity distribution and pore size distribution of a sub-sample of the column, is able to reproduce the experimentally observed solute breakthrough curves. Pore-scale modelling provided the extent of pore velocity variations corresponding to various locations along the experimental column as well as the one dimensional (1D) Darcy scale model. We have found that even in homogenous porous media immobile pores exist, with low velocities compared to the average velocity, which creates local concentration maximals.

1. Introduction

Solute dispersion in porous media has been the focus of many systematic studies in various fields of hydrology, geophysics, petroleum engineering, chemical engineering, soil physics, and agricultural engineering (Bijeljic et al., 2013; Delgado, 2006). Dispersion plays a key role in subsurface transport by affecting the migration of contaminants, the mixing of salt and fresh water (Nick et al., 2013), and related processes. Over the past decades, solute dispersion phenomena have been widely investigated theoretically, experimentally, and numerically from the pore scale to the column scale and the field scale under both saturated and unsaturated conditions (Agrawal et al., 2020; Bunsri et al., 2008; Dünser and Meyer, 2016; Estabragh et al., 2013; Harvey and Gorelick, 1995; Kohanpour et al., 2020; McDaniel et al., 2015; Raoof and Hassanizadeh, 2013; Sherman et al., 2018; Toride et al., 2003; Zhen et al., 2016). The degree of solute spreading has been found to be closely related to the water flow velocity distribution within and between pores, the divergence and convergence of flow paths within the porous medium, and molecular diffusion (see "Theory of solute dispersion in porous media" in Supplementary Materials) (Delgado, 2006;

Harvey and Gorelick, 1995). Furthermore, dispersivity is known to be a scale dependent parameter, which increases with the length scale, providing subsurface solute transport studies with a great challenge.

Transport of solutes at the field scale involves difficulties due to the inherent uncertainty in subsurface hydraulic and transport parameters. Subsurface heterogeneity at the field scale of aquifers is one of the most uncontrolled parameters that has a significant effect on solute transport, particularly for reactive solutes (Nick et al., 2011; Pu and Fox, 2015; Slimene et al., 2015). Although column scale experiments in the laboratory allow much more control over the experimental conditions, they are generally still too macroscopic in nature to directly observe the contribution of the underlying pore-scale processes on flow, solute transport and spreading. Nevertheless, investigating these underlying processes at the microscopic or pore scale offers a unique way to study the scale dependency of continuum-scale transport parameters. Such scale dependency cannot be easily captured by an effective medium Darcy approach (Bultreys et al., 2016; Xiong et al., 2016). For this reason, pore scale information can be valuable for understanding solute dispersion at the larger length scales (Delgado, 2006). Several studies indicate that pore scale modelling allows to relate the macroscale dispersion coefficient to the pore size distribution and velocity distribution within a porous medium (Bultreys et al., 2016; Xiong et al., 2016; Parvan et al., 2020). among existing methods, pore network modelling (PNM) has been increasingly used to simulate results from labora-

* Corresponding author at: Deparement of Earth Sciences, Utrecht University, Budapestlaan 4, 3584CD Utrecht, the Netherlands.
E-mail address: m.gharehmahmoodlu@uu.nl (M.G. Mahmoodlu).

tory experiments and to improve our understanding of underlying pore-scale processes (Bodla et al., 2010; Delgado, 2006; Köhne et al., 2011; Porta et al., 2016; Varloteaux et al., 2013). They are now widely used in the geosciences and related fields to study capillarity and multiphase flow (Bultreys et al., 2015; Zhou and Helland, 2016) non-reactive and reactive contaminant transport (Acharya et al., 2007; Delgado, 2006; Köhne et al., 2011; Varloteaux et al., 2013), mineral dissolution and precipitation processes caused by CO_2 sequestration (Algive et al., 2010; Nogues et al., 2013; Raoof et al., 2012), electrokinetic transport in charged porous media (Li et al., 2014; Zhang et al., 2015a) as well as colloid and virus transport (Seetha et al., 2014; Zhang et al., 2015b), among other applications.

Most or all of PNM studies thus far have been used to simulate fluid flow and/or solute transport processes in natural and engineered porous media at relatively small spatial scales, generally from a mm to at most a few cm (Mehmani and Balhoff, 2015; Yang et al., 2016). Few if any studies exist where the models have been applied to larger length scales (e.g., 30 cm or larger) due to limitation of imaging techniques to acquire large 3D pore networks and the required computational times to simulate the governing equations of flow and transport in the resulting media. Simulating pore scale processes on larger length scales should help to improve our understanding needed to explain the dependency of scale-variant transport parameters on travel distance and various pore scale properties (e.g., coordination number and pore size). Moreover, the results would significantly help to develop macroscale constitutive relationships suitable as inputs for continuum scale models for a wide range of applications as explained earlier.

1.1. Pore-scale modelling

Various pore scale computational methods have been developed to study flow and transport through porous media. Some directly simulate transport on the complex pore geometry and some simulate using a conceptualized pore network that retains the same topological structure of the media (Yang et al., 2016). The first type of model is typically referred to as direct numerical simulation which includes standard computational fluid dynamics, for example, lattice Boltzmann method (Chen et al., 2018; Zhou et al., 2020; Parvan et al., 2020), smoothed particle hydrodynamics (Tartakovsky et al., 2016; Ye et al., 2019), or finite element methods to directly solve the pore-scale governing equations (Agrawal et al., 2020). The second presents the pore space as a connected network with geometrically simplified pore bodies and pore throats and applies a Eulerian description (e.g., Raoof et al., 2013) or a Lagrangian method (e.g., Bijeljic et al., 2004) to obtain transport though the media over time. This method intends to maintain the topology of the actual pore space but does not represent the geometric details of individual pores/throats to gain computational efficiency (Dong and Blunt, 2009; Raoof and Hassanizadeh, 2010; Yang et al., 2016).

1.2. X-ray tomography (CT scan)

To provide accurate results, a pore scale model should be able to reproduce the main geometric and topological features of the real porous medium, including the pore-size distribution and the connectivity between pores (Arns et al., 2004; Raoof and Hassanizadeh, 2010). The need for accurate pore structure makes non-destructive 3D imaging techniques, such as X-ray micro-computed tomography (micro-CT), valuable tools for quantifying the internal structure of porous media in three dimensions (Cnudde and Boone, 2013; Vaz et al., 2014; Wildenschild and Sheppard, 2013). The combination of 3D imaging together with image analysis provides the necessary information for pore scale modelling (Fig. 1).

X-ray micro-CT imaging is being used increasingly to investigate the internal structures of a large variety of porous objects including geomaterials (Boone et al., 2014; T. Bultreys et al., 2015; Cnudde and Boone, 2013; Griggs et al., 2015; Pereira et al., 2016). One of the most

common applications of X-ray tomography in subsurface research is the extraction of pore networks from micro-CT images of soil and rocks to allow investigations of pore-scale flow and reactive transport processes (Blunt et al., 2013; Boone et al., 2014; Bultreys et al., 2015a; Cnudde and Boone, 2013; Griggs et al., 2015; Pereira et al., 2016). Dynamic imaging experiments using micro-CT are now being used to investigate in-situ pore-scale processes at the mm to cm scale (Bultreys et al., 2015b; Menke et al., 2015). In this study, we use micro-CT together with image analysis techniques to extract a representative pore network of laboratory column-scale experiments, and to use the resulting pore network to simulate flow and tracer ($CaCl_2$) transport through the column.

1.3. Objectives

In this study, we intend to explore solute transport and dispersion using three different methods: column transport experiments, continuum-scale modelling, and pore-scale modelling. We performed a series of 36-cm long sand column transport experiments under saturated conditions to obtain solute breakthrough curves at several locations along the flow path, from which we calculate hydrodynamic dispersion coefficients using continuum scale modelling. At the same time, a representative part of the same sand sample was imaged using X-ray micro-CT to directly extract the pore network and to obtain the geometric and topological properties of the pore space. Since micro-CT has a sample size/resolution trade-off that significantly hinders direct imaging of the entire 36-cm sand column at the required resolution, the statistical properties of the accurate image-based pore network of the representative sample were used to construct a very large pore network model with a size equal to the sand column experiment (i.e., a 36-cm long pore scale domain). Fluid flow and solute transport were subsequently simulated in the large network to obtain both the 3D distribution of solute within the domain and the breakthrough curve of solutes at several locations identical to the experiments (11, 18, 25, 36 cm). This allowed us to directly compare solute dispersion processes based on the experimental data, continuum scale modelling, and pore network simulation.

2. Materials and methods

2.1. Experimental column

Fig. 2 shows a schematic of the experimental setup used in our study. A glass cylinder of 36 cm length and 9.0 cm internal diameter was used to construct the experimental column, which contained stainless steel lids with a port at its inlet and outlet faces. Three measuring probes at depths of 11, 18 and 25 cm were placed along the column to obtain solute concentrations utilizing the measured electrical conductivity (EC).

The column was packed with a well-sorted filtered sand originating from a river bed in Papendrecht, the Netherlands (Filtersand, Filcom, Netherlands). The filter sand had an average grain size (i.e., the D_{50} value) of 0.50 mm, with the grain size varying mostly between 0.43 and 0.63 mm. Selected properties of the sand sample are given in Table 1. The columns were packed and provided a porosity value of around 0.38. The porosity was calculated gravimetrically. After packing, the sand columns were flushed with CO_2 for a period of four hours to replace air from the soil pore spaces (due to high solubility of CO_2 in water respect to air), thus ensuring as water saturated as possible conditions. Next, the sand column was gradually saturated by water from the bottom using a peristaltic pump (Ismatec, Switzerland).

We established constant flow rates, ranging from 2.0 to 5.3 cm^3 min^{-1}, by adjusting the hydraulic head at the top of the sand column using a small water container. After reaching fully saturated steady state flow conditions, we applied a pulse input of a solute using a low concentration (0.05 M) of $CaCl_2$ (Sigma-Aldrich). Dynamic measurement of soil moisture, temperature, and EC were carried out over time using several 5TE sensor (See "Measurements" in Supplementary Materials).
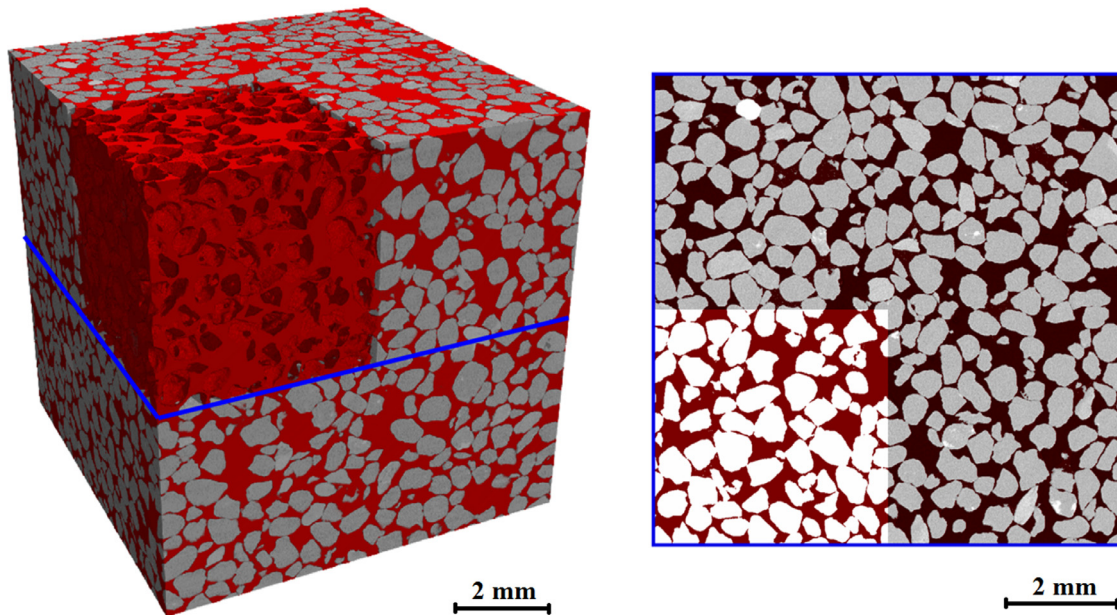
Fig. 1. 3D and 2D rendering of the segmented pore structure (red) on top of the original CT data (grey). The segmentation was performed using a K-means clustering algorithm, whereas the 3D render was constructed in VGStudio.
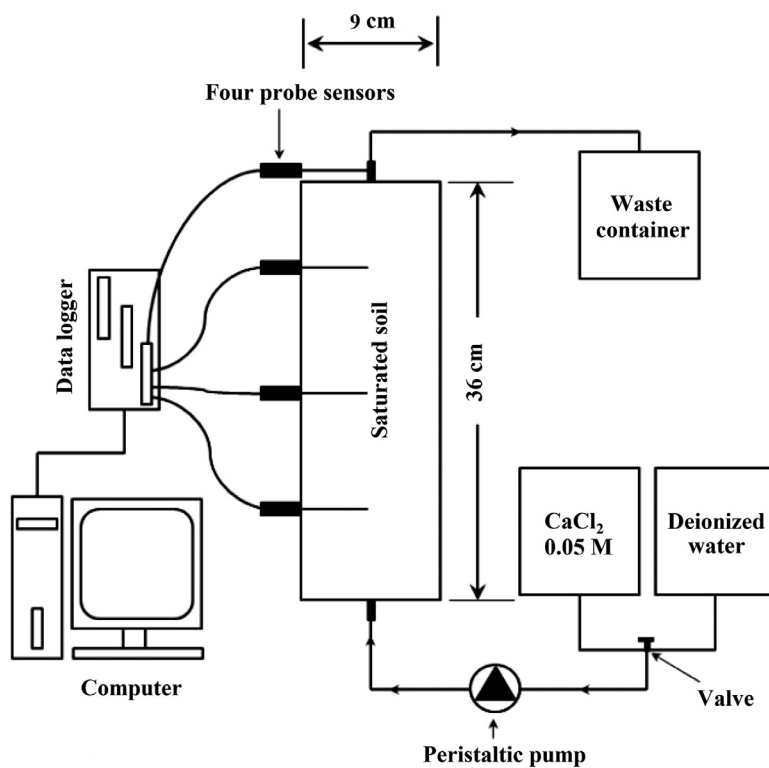

Fig. 2. Schematic figure of the experimental setup and sand columns used in this study.

2.2. Micro-CT imaging of sand samples

A sand sub-sample was taken from the experimental column using a plastic tube of 5 cm long and 1.5 cm inner diameter with sharp edges. To prevent any displacements of sand grains, the sample was partially saturated. This resulted in the adhesion of sand particles. The three-dimensional pore structure of the subsample was measured with the HECTOR micro-CT scanner at UGCT, Ghent, Belgium (Masschaele et al., 2013). The sample was scanned with an accelerating voltage of 100 kV and a target power of 10 W. 2400 projections (1 s illumination each) were reconstructed using Octopus Reconstruction software (Inside Matters, Belgium), resulting in a 3D dataset with a voxel size of (8.3 μm) (Nick et al., 2013).

2.3. Pore network modelling (PNM) of flow and transport in a saturated sand column

To directly compare the breakthrough curves obtained experimentally with PNM results, a pore network must be constructed with the same length as the experimental columns (i.e., 36 cm in this study).

Table 1
Properties of the sand used in this study.

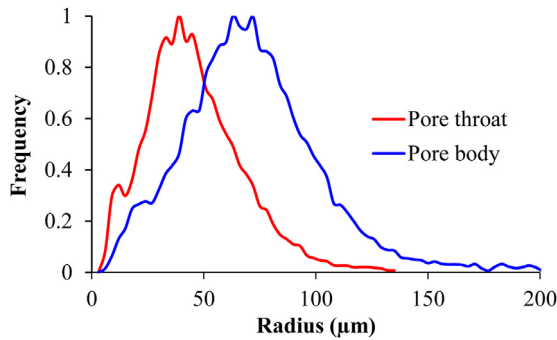| Parameters	Value
Density (g/cm³)	2.58
pH (1:1 water)	7.00
Grain shape	Subrounded & Subangular
TOC (%)	0.05
D_{50} (mm)	0.50
D_{10} (mm)	0.43
C_u	1.10
C_c	1.01

[1]D_{10}: effective diameter of sand.
[2]D_{50}: medium diameter of sand.
[3]C_u: the coefficient of uniformity.
[4]C_c: coefficient of curvature.
[5]TOC: Total Organic Carbon in dry sample.

Fig. 3. Pore size distribution obtained from micro-CT 3D imaging.

It is not feasible to scan the complete 9.0 cm diameter experimental column since this would require lowering the micro-CT scan resolution and lead to less accurate pore structures. Even if the desired resolution could be maintained, scanning a 36-cm long column at a voxel pitch of 8.3 μm would require an extremely long scanning time and result in an impractically large micro-CT dataset. For this reason, we extracted the pore network from the imaged sub-sample and used this to construct an equivalent network for the entire 36-cm column that was statistically identical to the imaged sample.

To do so, the micro-CT scan was first segmented by automatically selecting a grey-value threshold using a K-means clustering algorithm. Spurious noise voxels were removed using a majority filter in Octopus Analysis (Brabant et al., 2011). The pore network domain was then extracted using a grain-recognition based network extraction algorithm using the eCore software (FEI, Norway) (Bakke and Øren, 1997).

To construct the larger and stochastically representative pore network, we targeted key geometrical and topological parameters of the sand pack, i.e., the pore size distribution, the pore connectivity distribution, and the pore throat lengths. These are the major controlling parameters for flow and solute transport and should therefore be the same for the larger-scale stochastic network as the direct image-based network. For the pore sizes, a large number of pore body and throat sizes were generated by applying the same pore size distribution obtained through imaging (Fig. 3). The pore coordination number distribution obtained from the image-based network was replicated in the stochastic model using the multi-directional random structure pore network developed by Raoof and Hassanizadeh (2010). This method uses an initial pore network with a high pore coordination number, and then eliminates pores to obtain a network with a desired average and distribution of the pore coordination number that matches the measured values from the image-based model.

A saturated flow field was established in the pore network by imposing different pressures on the opposing inlet and outlet boundaries of the network. All other boundaries parallel to the overall flow direc-
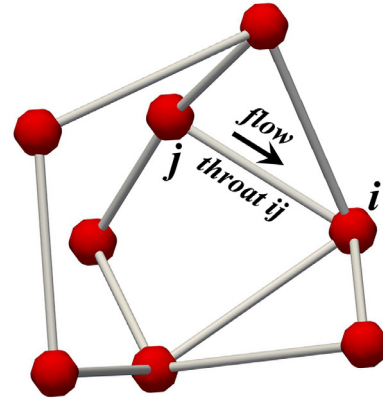
Fig. 4. Example of interconnected pore bodies and pore throats. Node j is the upstream node.

tion were assumed to be no-flow boundaries. Fig. 4 shows a schematic representation of pore bodies interconnected by means of pore throats within the network, with flow occurring from pore body j towards pore body i through pore throat ij. Such pore space discretization provides a computationally efficient way to solve flow and transport in porous media compared to the direct numerical solution of governing transport equations in complex pore structures (Fathi et al., 2017).

We assumed that discharge, q_{ij}, through a given pore throat can be prescribed by the Hagen-Poiseuille equation (Li et al., 2014; Raoof et al., 2012):

$$q_{ij} = \frac{\pi R_{ij}^4}{8\mu l}(P_j - P_i) \tag{1}$$

where q_{ij} is the volumetric discharge through pore throat ij, R_{ij} is the radius of the pore throat, μ is the dynamic viscosity, and P_i and P_j are pressures at pore bodies i and j, respectively. We assumed incompressible steady-state saturated flow such that the sum of discharges of all pore throats connected to a pore body must be zero:

$$\sum_{j=1}^{z_i} q_{ij} = 0 \qquad j = 1, 2, ..., z_i \tag{2}$$

where z_i is the coordination number of pore body i. Combining Eqs. (1) and (2) for all pores leads to a linear system of equations with a sparse, symmetric, positive-definite coefficient matrix, which can be solved for the pore body pressures. The flow velocities in all pore throats can be calculated using Eq. (1).

Considering the network as a REV, the average pore water velocity $\bar{v}$ is given by:

$$\bar{v} = \frac{QL}{V_f} = \frac{Q}{\phi A} \tag{3}$$

in which Q is the total flux (being the sum of fluxes through all pore throats at the inlet or outlet boundary of the network), L is the network length, V_f is total fluid volume in the network, φ is porosity, and A is the cross-sectional area of the sample perpendicular to the flow direction.

Solute transport through the pore network was calculated for both pore bodies and pore throats and considering advection and diffusion processes. Calculations were done by considering each pore element (i.e., the pore bodies and pore throats) as a control volume. The estimated pore velocities using Eq. (3) were used in calculations of the advection term in the solute transport equations. The solute concentration in a given pore body, i, was obtained using (Li et al., 2014; Raoof et al., 2012):

$$V_i \frac{dc_i}{dt} = \sum_{j=1}^{N_{in}^{th}} q_{ij}c_{ij} - Q_i c_i + \sum_{j=1}^{z_i} D_0 A_{ij} \frac{(c_{ij} - c_i)}{l_{ij}} \tag{4}$$

where V_i is the volume of pore body i, Q_i is the total volumetric volume rate going out of the pore body i, A_{ij} is the cross sectional area of the pore throat, D_0 is the ionic or molecular diffusion coefficient, c_i is the concentration in pore body i, c_{ij} is the concentration in the pore throat between pore bodies i and j, l_{ij} is again the length of that throat, and N_{in}^{th} is the number of pore throats flowing into the pore body i.

Assuming that pore body j is the upstream node and pore body i the downstream node, the solute concentration in pore throat ij can be obtained using (Raoof et al., 2012; Li et al., 2014):

$$V_{ij}\frac{dc_{ij}}{dt} = q_{ij}(c_j - c_{ij}) + D_0 A_{ij}\left(\frac{(c_j - c_{ij}) + (c_i - c_{ij})}{l_{ij}}\right) \quad (5)$$

Eq.s (4) and (5) were solved using a fully implicit method embedded in the PoreFlow package developed by Raoof et al. (2013). To obtain solute breakthrough curves, flux-averaged concentrations at selected distances were obtained by averaging concentrations over the network cross-section at successive times.

The applied pore network provided a total of 328,725 pores. This included 1461 pores in the x direction, along the sample length and the flow direction. At the cross-sectional plane (i.e., y and z directions) we have considered 15×15 pores which provides an area of 13.7 mm^2. This cross-sectional size was chosen based on the representative elementary volume (REV) size tested on the sample to provide stable values for porosity and permeability.

The computational time needed to get a full set of BTCs for each simulation using a fully implicit method (Raoof et al., 2013) was around 12 days using a parallelized program (shared memory multiprocessing using OpenMP architecture) on 6 cores under Linux OS.

3. Results and discussion

3.1. Breakthrough curves

The experimentally observed BTCs at four different depths are shown in Fig. 5 in terms of normalized concentrations (C/C_0) of CaCl$_2$. BTCs show a gaussian shape at all depths. This agrees with several studies of tracer transport in homogenously packed columns under saturated conditions (Lee et al., 2014; Toride et al., 2003). To describe the measured BTCs at the Darcy scale, we have assumed transport by advection and dispersion processes (see Section 1 in Supplementary Materials). Assuming a constant concentration at the inlet boundary (e.g., $\bar{C}(x = 0, t) = \bar{C}_{in}$) and a semi-infinite profile ($\frac{\partial \bar{C}}{\partial x}(\infty, t) = 0$), the analytical solution for the tracer distribution within the 1D column subject to a step increase of the inlet concentration from zero to $\bar{C}_o$ is given by:

$$\bar{C} = \bar{C}_o\left[\frac{1}{2}erfc\left(\frac{x - \bar{v}t}{2\sqrt{Dt}}\right) + \frac{1}{2}\exp\left(\frac{vx}{D}\right)erfc\left(\frac{x + \bar{v}t}{2\sqrt{Dt}}\right)\right] \quad (6)$$

where t is the time of sampling after the step change in the input concentration, and $erfc$ is the complementary error function. We fitted Eq. (6) to the measured concentration BTCs to determine pore velocity, v, and the solute dispersion, D, from which the solute dispersivity, λ, was calculated as $D = D_e + \lambda v^n$, where D_e is an effective diffusion coefficient [L^{2}T^{-1}], λ is the (longitudinal) dispersivity [L] which is assumed to be an intrinsic soil property for saturated flow, and n is a parameter. Here, we assumed the contribution of the molecular diffusion at high values of Péclet number ($P_e > 10$) is negligible and the empirical constant n in hydrodynamic dispersion equation is equal to one. The CXTFIT program was used to fit Eq. (6) to obtain the transport parameters (see "Theory of solute dispersion in porous media" in Supplementary Materials) (Toride et al., 1995). Fig. 5 shows excellent agreement between the macroscale BTC's and the experimental data. Results of the fitting parameters are provided in Table 2. R-squared values for regression of the observed data versus predicted data in all experiments was very high and around 0.98. Results of macro scale model at different locations show that the estimated dispersivity values increase with travel
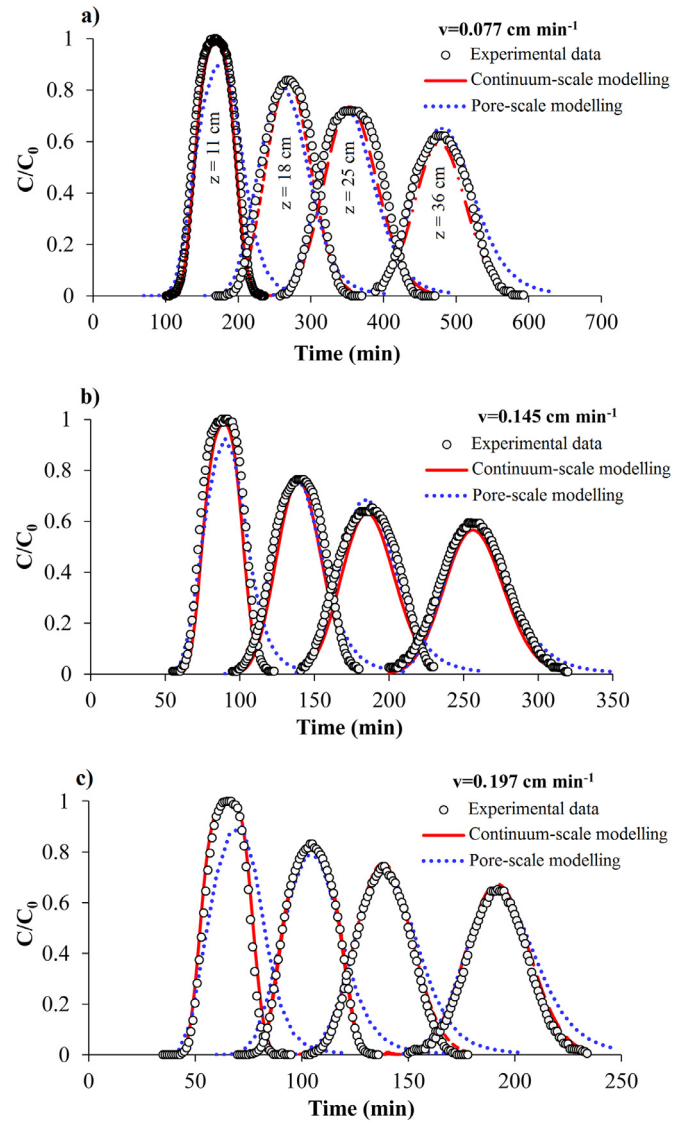
Fig. 5. Comparison of measured and simulated breakthrough curves (continuum scale model) and the PoreFlow pore scale results at four different depths (11, 18, 25, 36 cm) of the column. a): First experiment with velocity of 0.077 cm min^{-1}, b): Second experiment with velocity of 0.145 cm min^{-1}, and c) Third experiment with velocity of 0.197 cm min^{-1}. R-Squared for regression of observed vs predicted results for CM and PNM was about 0.98 and 0.961, respectively. For BTCs under $v = 0.145$ cm min^{-1}, the standard errors of residuals from fitting to the experimental data were equal to 0.0022 and 0.0031 for CM and PNM fits, respectively. A video clip of a simulation with velocity of 0.14 cm min^{-1} is provided in Supplementary Materials showing 3D distribution of concentrations as well as BTCs at three different locations.

distance to reach to asymptotic values at around a distance of 25 cm. Furthermore, dispersivity values slightly increase with the pore water velocity reduction (Fig. 6). However, the dispersivity at a short distance increases more over the travel distance when the velocity is smaller. These results are consistent with several earlier experimental studies using repacked soils showing dependency of the dispersivity on travel distance and pore water velocity (Appelo and Postma, 2004; Bandai et al., 2017; Bromly et al., 2007; Kanzari et al., 2015; Nützmann et al., 2002; Toride et al., 2003).

We have calculated the dimensionless Péclet number to evaluate the effect of molecular diffusion on the hydrodynamic dispersion. For the macro scale model, very high Péclet number ($P_e > 50$) values were obtained. This confirms the validity of our assumption that the contribu-

Table 2
Estimated parameters from the experimental BTC at each depth using a single-continuum model and a pore scale model.

Flow (cm³ min⁻¹)	L (cm)	Continuum model (CM)		Pore network model (PNM)		Δv	$\Delta \lambda$
		v_1 (cm min⁻¹)	λ_1 (cm)	v_2 (cm min⁻¹)	λ_2 (cm)		
1.9	11	0.079	0.0377	0.0794	0.1136	−0.0004	−0.0759
	18	0.0743	0.0921	0.0791	0.1244	−0.0048	−0.0323
	25	0.0787	0.1211	0.0794	0.1235	−0.0007	−0.0024
	36	0.076	0.1313	0.0813	0.1241	−0.0053	0.0072
	[a]Mean	0.077	0.0955	0.0798	0.1214	−0.0028	−0.0259
3.9	11	0.1449	0.0344	0.1361	0.1092	0.0088	−0.0748
	18	0.1449	0.0828	0.1355	0.1209	0.0094	−0.0381
	25	0.1449	0.1028	0.136	0.121	0.0089	−0.0182
	36	0.1449	0.1187	0.1389	0.121	0.006	−0.0023
	Mean	0.1449	0.0847	0.1366	0.118	0.0083	−0.0333
5.3	11	0.1969	0.0411	0.1984	0.1146	−0.0015	−0.0735
	18	0.1969	0.0706	0.1977	0.1257	−0.0008	−0.0551
	25	0.1969	0.0914	0.1984	0.1252	−0.0015	−0.0338
	36	0.1969	0.1011	0.2032	0.1262	−0.0063	−0.0251
	Mean	0.1969	0.0761	0.1994	0.1229	−0.0025	−0.0468

[a] : Mean value within column; v_1 and v_2: are the velocity calculated from a continuum model (CM) and pore network model (PNM), respectively; λ_1 and λ_2 are the dispersivity calculated from a CM and PNM, respectively; Δv: velocity difference between the CM and PNM; $\Delta \lambda$: dispersivity difference between the CM and PNM.
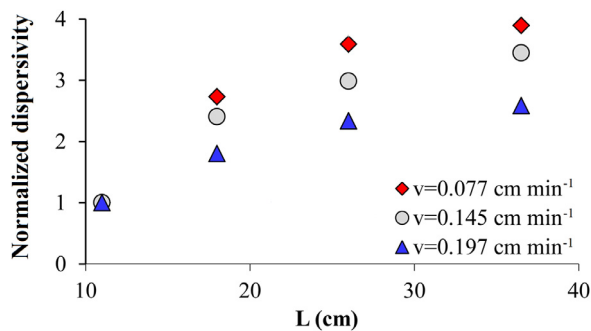
Fig. 6. Normalized dispersivity values of the continuum model (CM) obtained as a function of depth (L) for three different velocity values. Dispersivity values were normalized relative to the dispersivity at a depth of 11 cm.

tion of the molecular diffusion is negligible, and the empirical constant n is equal to one. Results also showed that with an increase in the Péclet number and/or velocity, the longitudinal dispersion coefficient increased. These results are consistent with earlier studies (see Fig 1, Supplementary Materials).

3.2. Pore network results

The process of generating a larger pore network having a size equal to the 36 cm-column experiment was explained in Section 2.3. For initial and boundary conditions, we have considered similar situations as those applied to column experiments. The macroscopic 1D model uses one average velocity for each experiment. The corresponding pore scale models is, however, three-dimensional where different pores have different velocities. The average of pore velocities should be equal to the macroscopic 1D velocity in order to compare the two different-scale models. To obtain target average velocities we have assigned different pressures at the inlet and outlet faces of the pore network model and calculated the steady-state flow by solving Eqs. (1) and (2) using PoreFlow (to obtain velocity values of 0.077, 0.145, and 0.197 cm min⁻¹). Similar to the experiments, the initial concertation of the pores was set to zero in the pore network model. A pulse injection of solute was stimulated by setting the pore concentrations at the inlet face of the network to $C/C_0 = 1.0$ for a period of time followed by injecting solute-free water

(i.e., $C/C_0 = 0.0$) for the rest of simulation. During the simulation, the concentration of pores located at the outlet of the pore network was averaged (i.e., cross sectional average weighted by velocity of pores) at different times to obtain the time-curve of average outlet concentration which is compatible with the concentration measurements at the outlet of column experiments. The resulting BTCs from PNM simulations are shown in Fig. 5 together with the BTCs obtained from experiments and the 1D macroscale model. In general, PNM could simulate the experimental BTCs. Transport parameters used in PNM are provided in Table 2. Fig. 5 shows that, compared to the Darcy model, PNM provides a less quality fit to the experimental observations. This difference can be explained based on the scale of the two models (which determines their mathematical formulations) and the level of complexity that they include. Darcy scale model assumes flow and transport in the column as 1D macroscopic processes. Consequently, it applies one (average) velocity and uses a dispersion coefficient to account for solute mixing. The dispersion coefficient is a fitting parameter and is tuned to obtain the best possible fit (i.e., the Darcy model fit in Fig. 5). Since the column is homogenous the fit quality is very good. The pore scale model, however, included the complex 3D pore structure of the media and simulates flow and transport in three-dimensional space. This model simulates the experimental observations without using any fitting transport parameter (unlike Darcy model that uses dispersion coefficient as a fitting coefficient). As pore structures in porous media are often very complex, and there is no assumption of 1D flow or presence of a fitting parameter, the quality of the agreement between pore-scale modelling results and the experimental observations may not be very good. The degree of agreement depends on the ability of the chosen pore-scale model to represent 3D pore structures. It is possible to use numerical simulations which capture details of the 3D pore structures (such as direct numerical solution of the Navier-Stokes equations). However, such as simulations are computationally very expensive and cannot be used for simulations in long columns such as the 36-cm length column used in this study. Pore network modelling enables simulating such a large column, however, simplifies the pore structures into a network of pore bodies and pore throats. The quality of pore-scale BTCs are better at locations farther from the inlet of the sample (Fig. 5). The generated pore network model was macroscopically homogenous, with the pore sizes obtained from imaging. Since the soil column was uniformly packed and carefully filled cm by cm, the medium should be macroscopically homogenous. Therefore, PNM tailing of short-distance BTCs may be due to its for-
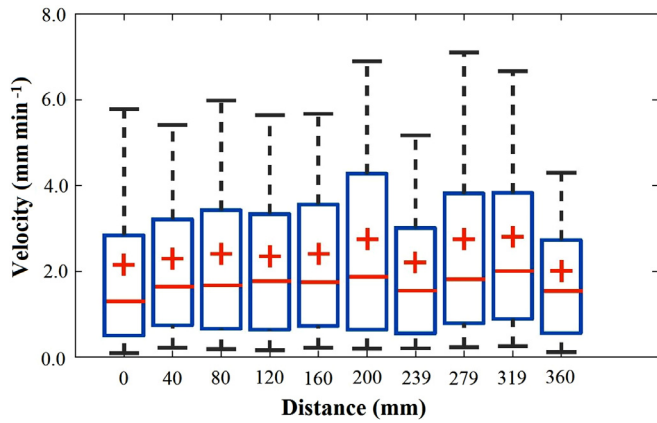
Fig. 7. Variations of pore water velocities at 10 different locations along the sand column using pore network modelling. Whiskers show 9% and 91% velocity bounds. The central orange marks show the medians and the edges of the boxes the 25th and 75th percentiles. Here, flow rate was 3.9 cm^3 min^{-1}.

ficult to be obtained experimentally in long columns. The Darcy model provides a dispersion coefficient as an indication of velocity variations. The pore scale model, however, provides pore-level velocity variations within the sample and shows how different pores with different velocities contribute to solute transport. Pore-scale simulations indicate that by relatively advection-dominant conditions, local flow velocity variations are the main cause of solute dispersion. To present velocity variations, we have averaged pore velocity values of pore throats at several cross sections along the sample and provides the statistical information for each location. The velocities are obtained by dividing the volumetric flux of each pore throat located at the chosen cross section by its cross-sectional area.

Fig. 7 shows the analysis of velocity variations. There is a wide range of velocities at different cross sections of the column with some pores having a nearly 5 times higher velocity compared to the average velocity of the column experiments and several pores having very low velocity values.

Our results shown that pore scale concentration values have a slightly positive correlation with the pore coordination number. This can be explained based on the higher connectivity of pores with larger coordination numbers, and the concomitant larger water and solute fluxes through these pores.

In continuum scale modelling, the solute dispersive fluxes are simulated using values of concentration gradients. This leads to classical monotonically increasing concentration values behind the BTC peak, and to monotonically decreasing concentration values ahead of the BTC peak (Fig. 8a). Such a 1D concentration distribution is indeed the behaviour of the cross-sectional average of the 3D pore scale concentrations over time (Fig. 8(a) and (b)). However, remarkably, Fig. 8c illustrates that in contrast to the continuum scale modelling results, which provide monotonically changing concentrations behind and ahead of the BTC peak, there are several pores with much higher concentration values as compared to their surrounding pores (i.e., creating locally non-monotonic concentration variations). Our results have shown that such pores are often those with lower flow velocity values which create a relatively immobile liquid phase locally where the accumulated solute slowly diffuses back after the peak concentration passes. Fig. 8 shows that even in a homogenous porous medium several pores exist with very low velocities. As the fraction of such pores is smaller than the fraction
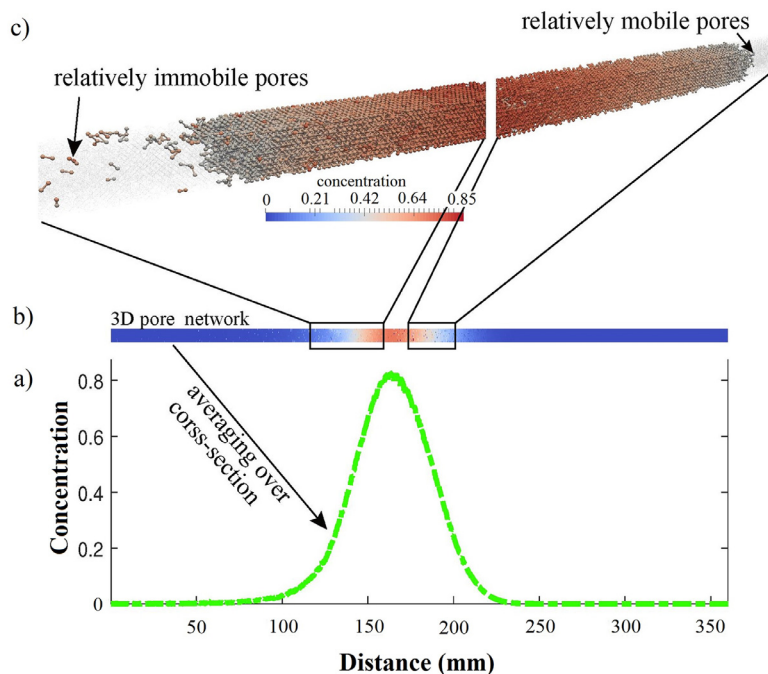
mulation that only one (average) pressure and concentration value is assigned to each single pore to enable simulations of relatively large domains. Although PoreFlow calculates separate concentrations for pore bodies and pore throats to lower solute mixing, the instant mixing within each pore element can overestimate the overall solute dispersion in the pore network. This effect should be more pronounced for relatively short travel times (i.e., close to the inlet) since then still larger concentration gradients are present. As solutes percolate further into the sample and experiences different pore spaces, concentration gradients become less abrupt, thus reducing the averaging effect. This is likely to be the reason for the better match of computed and measured BTCs obtained at longer distances. In contrast with dispersivity values derived from the measured BTCs, dispersivity values obtained with the PNM (0.109 cm to 0.121 cm) were almost constant with travel distance for the experiment with flow rate of 3.9 cm^3 min^{-1}.

The results obtained from Darcy model and pore-scale model are also different. Given the applied flow velocities, the cause of solute dispersion in our column experiments is velocity variations which are very dif-

Fig. 8. Profile of the average (1D) concentration along the sample (a) obtained by cross-sectional averaging the 3D pore scale concentrations (b). Plot c provides pore scale concentration distributions behind and ahead of the BTC for concentrations ranging between the peak concentration value and half the peak value. Here, flow rate was 3.9 cm^3 min^{-1}.

of the rest of pores within he sample, cross-sectional averaging provides concentrations values which are monotonies (i.e., Fig. 8a).

When the fraction of the relatively immobile pores is much larger one may choose to apply a mobile-immobile model (MIM) to simulate solute transport at the continuum scale. In our study, the column was packed very homogenously, and the fraction of immobile pores is low enough to allow the use of ADE model and to prevent extra terms needed when using MIM model. This choice is confirmed by the ability of the ADE model to fit the experimental BTCs very well (as shown in Fig. 5).

4. Conclusions

In this study, we investigated solute transport and dispersion using three complementary methods, including i) column-scale solute transport experiments to provide concentration measurements, ii) a 1D continuum-scale modelling to provide the macroscopic behaviour of the sand column and its dispersion coefficient, and iii) a pore-scale modelling to obtain the underlying velocity variations within the 3D pore structures which are responsible for the observed solute dispersion. For the first time it was shown that pore network modelling is able to simulate transport in a porous media in size of tens of centimetres. This provides confidence that this pore-scale approach can ultimately be applied to model the progress of reactive solutes along the length of shallow unsaturated zone and especially to depths where agricultural processes occur. The main findings can be summarized as follows:

1. We have shown that a pore network which matches both pore connectivity distribution and pore size distribution of the sample is able to reproduce the experimentally observed solute breakthrough curves. Therefore, there is no need to image the whole sample which is very challenging for long sample sizes such as the one used in this study. We should note that our soil column was homogeneous and the sub-sample used for imaging was larger than the size of the representative elementary volume (REV) which provide statistically stable transport parameters.

2. Ability to build a very long (36 cm) pore-scale model allowed us to directly compare the pore-scale modelling results with the experimentally measured solute concentrations as well as the results from continuum (Darcy) scale modelling. We found that even in a homogenous porous media immobile pores exist with low velocities compared to the average velocity. This process created local variations in the concentration field where several pores have much higher concentration values as compared to their surrounding pores. Such local concentration variations cannot be obtained when using continuum scale models as they lead to the classical monotonically increasing concentration values behind the BTC peak, and to monotonically decreasing concentration values ahead of the BTC peak.

3. Results show that the calculated dispersivity values increase with travel distance, as well as slightly increase with the pore water velocity reduction. Pore scale concentration values showed a slightly positive correlation with the pore coordination number. This may be explained based on the higher connectivity of pores with larger coordination numbers, and the concomitant larger fluxes through these pores.

Findings of this work will be helpful to illustrate the underlying processes contributing to the spread of a contaminant plume about the advective front. Such an understanding can contribute to the design of more cost-effective and accurate treatment schemes in natural settings by decreasing the uncertainties about the dispersion coefficient as well as the design of engineered permeable reactive barriers through choice of materials with optimum pore size distributions. Still, we acknowledge that more studies are needed for these applications, including the use of reactive solutes and more heterogeneous porous media.

Appendix. Supplementary materials

Video clip of a simulation with velocity of 0.145 cm min-1 showing 3D distribution of concentrations as well as BTCs at three locations. Note: to provide a better visualization, the model cross section in this video is reduced to 10×10 pores while the domain length is kept unchanged to represent 36 cm of the sand sample.

Declaration of Competing Interest

The authors declare that they have no known competing financial interests or personal relationships that could have appeared to influence the work reported in this paper.

CRediT authorship contribution statement

Mojtaba G. Mahmoodlu: Conceptualization, Data curation, Formal analysis, Investigation, Project administration, Methodology, Writing - original draft, Writing - review & editing. **Amir Raoof:** Supervision, Resources, Software, Writing - review & editing, Funding acquisition. **Tom Bultreys:** Software, Visualization. **Jeroen Van Stappen:** Software, Visualization. **Veerle Cnudde:** Writing - review & editing.

Acknowledgments

Supplementary materials

Supplementary material associated with this article can be found, in the online version, at doi:10.1016/j.advwatres.2020.103713.

References

Acharya, R.C., Valocchi, A.J., Werth, C.J., Willingham, T.W., 2007. Pore-scale simulation of dispersion and reaction along a transverse mixing zone in two-dimensional porous media. Water Resour. Res. 43 (10).

Agrawal, P., Raoof, A., Iliev, O., Wolthers, M., 2020. Evolution of pore-shape and its impact on pore conductivity during CO_2 injection in calcite: single pore simulations and microfluidic experiments. Adv. Water Resour. 136, 103480.

Algive, L., Bekri, S., Vizika, O., 2010. Pore-network modeling dedicated to the determination of the petrophysical-property changes in the presence of reactive fluid. SPE J. 15 (03), 618–633.

Appelo, C.A.J., Postma, D., 2004. Geochemistry, Groundwater and Pollution. CRC press.

Arns, J., Robins, V., Sheppard, A., Sok, R., Pinczewski, W., Knackstedt, M., 2004. Effect of network topology on relative permeability. Transp. Porous Media 55, 21–46.

Bakke, S., Øren, P., 1997. 3-D Pore-scale modelling of sandstones and flow simulations in the pore networks. SPE J 2, 136–149.

Bandai, T., Hamamoto, S., Rau, G.C., Komatsu, T., Nishimura, T., 2017. The effect of particle size on thermal and solute dispersion in saturated porous media. Int. J. Therm. Sci. 122, 74–84.

Bijeljic, B., Muggeridge, A.H., Blunt, M.J., 2004. Pore-scale modeling of longitudinal dispersion. Water Resour. Res. 40 (11).

Bijeljic, B., Raeini, A., Mostaghimi, P., Blunt, M.J., 2013. Predictions of non-Fickian solute transport in different classes of porous media using direct simulation on pore-scale images. Phys. Rev. E 87 (1).

Blunt, M.J., Bijeljic, B., Dong, H., Gharbi, O., Iglauer, S., Mostaghimi, P., Paluszny, A., Pentland, C., 2013. Pore-scale imaging and modelling. Adv. Water Resour. 51, 197–216.

Bodla, K.K., Murthy, J.Y., Garimella, S.V., 2010. Resistance network-based thermal conductivity model for metal foams. Com. Mater. Sci. 50 (2), 622–632.

Boone, M.A., De Kock, T., Bultreys, T., De Schutter, G., Vontobel, P., Van Hoorebeke, L., Cnudde, V., 2014. 3D mapping of water in oolithic limestone at atmospheric and vacuum saturation using X-ray micro-CT differential imaging. Mater Charact 97, 150–160.

Brabant, L., Vlassenbroeck, J., De Witte, Y., Cnudde, V., Boone, M.N., Dewanckele, J., Van Hoorebeke, L., 2011. Three-dimensional analysis of high-resolution X-Ray computed tomography data with Morpho+. Microsc. Microanal 17, 252–263.

Bromly, M., Hinz, C., Aylmore, L.A.G., 2007. Relation of dispersivity to properties of homogeneous saturated repacked soil columns. Eur. J. Soil Sci. 58 (1), 293–301.

Bultreys, T., Boone, M.A., Boone, M.N., De Schryver, T., Masschaele, B., Van Hoorebeke, L., Cnudde, V., 2015a. Fast laboratory-based micro-computed tomography for pore-scale research: illustrative experiments and perspectives on the future. Adv. Water Resour. 95, 341–351.

Bultreys, T., De Boever, W., Cnudde, V., 2016. Imaging and image-based fluid transport modeling at the pore scale in geological materials: a practical introduction to the current state-of-the-art. Earth-Sci. Rev. 155, 93–128.

Bultreys, T., Van Hoorebeke, L., Cnudde, V., 2015b. Multi-scale, micro-computed tomography-based pore network models to simulate drainage in heterogeneous rocks. Adv. Water Resour. 78, 36–49.

Bunsri, T., Sivakumar, M., Hagare, D., 2008. Numerical modelling of tracer transport in unsaturated porous media. J. App. Fluid Mech. 1 (1), 62–70.

Chen, L., Zhang, R., Min, T., Kang, Q., Tao, W., 2018. Pore-scale study of effects of macroscopic pores and their distributions on reactive transport in hierarchical porous media. Chem. Eng. J. 349, 428–437.

Cnudde, V., Boone, M.N., 2013. High-resolution X-ray computed tomography in geosciences: a review of the current technology and applications. Earth-Sci. Rev. 123, 1–17.

Delgado, J.M.P.Q., 2006. A critical review of dispersion in packed beds. Heat Mass Transf. 42 (4), 279–310.

Dong, H., Blunt, M.J., 2009. Pore-network extraction from micro-computerized-tomography images. Phys. Rev. E. 80 (3), 036307–036311.

Dünser, S., Meyer, D.W., 2016. Predicting field-scale dispersion under realistic conditions with the polar Markovian velocity process model. Adv. Water Resour. 92, 271–283.

Estabragh, A.R., Pereshkafti, M.R.S., Javadi, A.A., 2013. Comparison between analytical and numerical methods in evaluating the pollution transport in porous media. Geotech. Geol. Eng. 31 (1), 93–101.

Fathi, H., Raoof, A., van Genuchten, M.T., 2017. Effects of porosity and water saturation on the effective diffusivity of a cathode catalyst layer. J. Electrochem. Soc. 164 (4), 298–305.

Griggs, A.J., Davies, S.M., Abbott, P.M., Coleman, M., Palmer, A.P., Rasmussen, T.L., Johnston, R., 2015. Visualizing tephra deposits and sedimentary processes in the marine environment: the potential of X-ray microtomography. Geochem. Geophys. Geosyst. 16 (12), 4329–4343.

Harvey, C.F., Gorelick, S.M., 1995. Temporal moment-generating equations: modeling transport and mass transfer in heterogeneous aquifers. Water Resour. Res. 31 (8), 1895–1911.

Kanzari, S., Hachicha, M., Bouhlila, R., 2015. Laboratory method for estimating solute transport parameters of unsaturated soils. Geochem. Geophys. Geosyst. 1 (4), 151–156.

Kohanpur, A.H., Rahromostaqim, M., Valocchi, A.J., Sahimi, M., 2020. Two-phase flow of CO$_2$-brine in a heterogeneous sandstone: characterization of the rock and comparison of the lattice-Boltzmann, pore-network, and direct numerical simulation methods. Adv. Water. Resour. 135, p103469.

Köhne, J.M., Schlüter, S., Vogel, H.J., 2011. Predicting solute transport in structured soil using pore network models. Vadose Zone J. 10 (3), 1082–1096.

Lee, M.J., Hwang, S.I., Ro, H.M., 2014. Interpreting the effect of soil texture on transport and removal of nitrate-N in saline coastal tidal flats under steady-state flow condition. Cont. Shelf. Res. 84, 35–42 2014.

Li, S., Raoof, A., Schotting, R., 2014. Solute dispersion under electric and pressure driven flows; pore scale processes. J. Hydrol. 517, 1107–1113.

Masschaele, B., Dierick, M., Van Loo, D., Boone, M.N., Brabant, L., Pauwels, E., Cnudde, V., Van Hoorebeke, L., 2013. HECTOR: a 240kV micro-CT setup optimized for research. J. Phys. Conf. Ser. 463, 012012. https://doi.org/10.1088/1742-6596/463/1/012012.

McDaniel, J.P., Butters, G., Barbarick, K.A., Stromberger, M.E., 2015. Effects of on soil hydraulic properties and solute dispersivity. Soil Sci. Soc. Am. J. 79 (3), 838–847.

Mehmani, Y., Balhoff, M.T., 2015. Mesoscale and hybrid models of fluid flow and solute transport. Rev. Mineral Geochem. 80, 433–459.

Menke, H.P., Bijeljic, B., Andrew, M.G., Blunt, M.J., 2015. Dynamic three-dimensional pore-scale imaging of reaction in a carbonate at reservoir conditions. Environ. Sci .Technol. 49 (7), 4407–4414.

Nick, H.M., Paluszny, A., Blunt, M.J., Matthai, S.K., 2011. Role of geomechanically grown fractures on dispersive transport in heterogeneous geological formations. Phys. Rev. E 84 (5), 056301–056309.

Nick, H.M., Raoof, A., Centler, F., Thullner, M., Regnier, P., 2013. Reactive dispersive contaminant transport in coastal aquifers: numerical simulation of a reactive Henry problem. J. Contam. Hydrol. 145, 90–104.

Nogues, J.P., Fitts, J.P., Celia, M.A., Peters, C.A., 2013. Permeability evolution due to dissolution and precipitation of carbonates using reactive transport modeling in pore networks. Water Resour. Res. 49 (9), 6006–6021.

Nützmann, G., Maciejewski, S., Joswig, K., 2002. Estimation of water saturation dependence of dispersion in unsaturated porous media: experiments and modelling analysis. Adv. Water Resour. 25 (5), 565–576.

Parvan, A., Jafari, S., Rahnama, M., Raoof, A., 2020. Insight into particle retention and clogging in porous media; a pore scale study using lattice Boltzmann method. Adv. Water Resour. 138, 103530.

Porta, G.M., Ceriotti, G., Thovert, J.F., 2016. Comparative assessment of continuum-scale models of bimolecular reactive transport in porous media under pre-asymptotic conditions. J. Contam. Hydrol. 185, 1–13.

Pereira Nunes, J.P., Blunt, M.J., Bijeljic, B., 2016. Pore-scale simulation of carbonate dissolution in micro-CT images. J. Geophys. Res. Solid Earth 121, 558–576.

Pu, H., Fox, P.J., 2015. Model for Coupled Large Strain Consolidation and Solute Transport in Layered Soils. Int. J. Geomech. 04015064.

Raoof, A., Hassanizadeh, S.M., 2010. A new method for generating pore-network models of porous media. Transp. Porous Media 81 (3), 391–407.

Raoof, A., Hassanizadeh, S.M., 2013. Saturation-dependent solute dispersivity in porous media: pore-scale processes. Water Resou. Res. 49 (4), 1943–1951.

Raoof, A., Nick, H.M., Hassanizadeh, S.M., Spiers, C.J., 2013. PoreFlow: a complex pore-network model for simulation of reactive transport in variably saturated porous media. Comput. Geosci. 160–174.

Raoof, A., Nick, H.M., Wolterbeek, T.K.T., Spiers, C.J., 2012. Pore-scale modeling of reactive transport in wellbore cement under CO$_2$ storage conditions. Int. J. Greenh. Gas Con. 11, S67–S77.

Seetha, N., Kumar, M.M., Hassanizadeh, S.M., Raoof, A., 2014. Virus-sized colloid transport in a single pore: model development and sensitivity analysis. J. Contam. Hydrol. 164, 163–180.

Sherman, T., Foster, A., Bolster, D., Singha, K., 2018. Predicting downstream concentration histories from upstream data in column experiments. Water Resour. Res 54 (11), 9684–9694.

Slimene, E.B., Lassabatere, L., Winiarski, T., Gourdon, R., 2015. Modelling water infiltration and solute transfer in a heterogeneous vadose zone as a function of entering flow rates. J. Water Resource Prot. 7 (13), 1017.

Tartakovsky, A.M., Trask, N., Pan, K., Jones, B., Pan, W., Williams, J.R., 2016. Smoothed particle hydrodynamics and its applications for multiphase flow and reactive transport in porous media. Computat. Geosci. 20 (4), 807–834.

Toride, N., Inoue, M., Leij, F.J., 2003. Hydrodynamic dispersion in unsaturated dune sand. Soil Sci. Soc. Am. J. 67 (3), 703–712.

Toride, N., Leij, F.J., Van Genuchten, M.T., 1995. The CXTFIT code for estimating transport parameters from laboratory or field tracer experiments, 2(1).

Varloteaux, C., Békri, S., Adler, P.M., 2013. Pore network modelling to determine the transport properties in presence of a reactive fluid: from pore to reservoir scale. Adv. Water Resour. 87–100.

Vaz, C.M.P., Tuller, M., Lasso, P.R.O., Crestana, S., et al., 2014. New perspectives for the application of high-resolution benchtop X-Ray MicroCT for quantifying void, solid and liquid phases in soils. In: Teixeira, W.G., et al. (Eds.), Application of Soil Physics in Environmental Analyses: Measuring, Modelling and Data Integration, Progress in Soil Science. Springer Int. Publ., Switzerland, pp. 261–281. https://doi.org/10.1007/978-3-319-06013-2_12.

Wildenschild, D., Sheppard, A.P., 2013. X-ray imaging and analysis techniques for quantifying pore-scale structure and processes in subsurface porous medium systems. Adv. Water. Resour. 51, 217–246.

Xiong, Q., Baychev, T.G., Jivkov, A.P., 2016. Review of pore network modelling of porous media: experimental characterisations, network constructions and applications to reactive transport. J. Contam. Hydrol. 192, 101–117.

Yang, X., et al., 2016. Intercomparison of 3D pore-scale flow and solute transport simulation methods. Adv. Water Resour 95, 176–189.

Ye, T., Pan, D., Huang, C., Liu, M., 2019. Smoothed particle hydrodynamics (SPH) for complex fluid flows: recent developments in methodology and applications. Phys. Fluids 31 (1), 011301.

Zhou, Y., Helland, J.O., 2016. Hatzignatiou D.G. Computation of three-phase capillary pressure curves and fluid configurations at mixed-wet conditions in 2D Rock Images. S.P.E. J. 21 (01), 152–169.

Zhang, Q., Raoof, A., Hassanizadeh, S.M., 2015a. Pore-Scale Study of Flow Rate on Colloid Attachment and Remobilization in a Saturated Micromodel. J. Environ. Qual. 44 (5), 1376–1383.

Zhang, W., Yao, J., Gao, Y., Zhang, Q., Sun, H., 2015b. Analysis of electrokinetic coupling of fluid flow in porous media using a 3-D pore network. J. Petrol. Sci. Eng. 134, 150–157.

Zhen, Q., Zheng, J., He, H., Han, F., Zhang, X., 2016. Effects of Pisha sandstone content on solute transport in a sandy soil. Chemosphere 144, 2214–2220.

Zhou, X., Xu, Z., Xia, Y., Li, B., Qin, J., 2020. Pore-scale investigation on reactive flow in porous media with immiscible phase using lattice Boltzmann method. J Petrol. Sci. Eng., 107224.